ACS NANO

www.acsnano.org

ARTICLE

Homogeneous Adsorption of Multiple Potassiation Products of Red Phosphorus Anode toward Stable Potassium Storage

Feiyue Wang, Tong Yang, Wencong Feng, Jingke Ren, Xingbao Chen, Chaojie Cheng, Wen Luo,* Xiaobin Liao,* and Liqiang Mai*

Cite This: *ACS Nano* 2024, 18, 17197−17208

Read Online

ACCESS | Metrics & More | Article Recommendations | Supporting Information

ABSTRACT: **Potassium ion batteries (PIBs) are a viable alternative to lithium-ion batteries for energy storage. Red phosphorus (RP) has attracted a great deal of interest as an anode for PIBs owing to its cheapness, ideal electrode potential, and high theoretical specific capacity. However, the direct preparation of phosphorus−carbon composites usually results in exposure of the RP to the exterior of the carbon layer, which can lead to the deactivation of the active material and the production of "dead phosphorus". Here, the advantage of the $\pi-\pi$ bond conjugated structure and high catalytic activity of metal phthalocyanine (MPc) is used to prepare MPc@RP/C composites as a highly stable anode for PIBs. It is shown that the introduction of MPc greatly improves the uneven distribution of the carbon layer on RP, and thus improves the initial Coulombic efficiency (ICE) of PIBs (the ICE of FePc@RP/C is 75.5% relative to 62.9% of RP/C). The addition of MPc promotes the growth of solid electrolyte interphase with high mechanical strength, improving the cycle stability of PIBs (the discharge-specific capacity of FePc@RP/C is 411.9 mAh g^{-1} after 100 cycles at 0.05 A g^{-1}). Besides, density functional theory theoretical calculations show that MPc exhibits homogeneous adsorption energies for multiple potassiation products, thereby improving the electrochemical reactivity of RP. The use of organic molecules with high electrocatalytic activity provides a universal approach for designing superior high-capacity, large-volume expansion anodes for PIBs.**

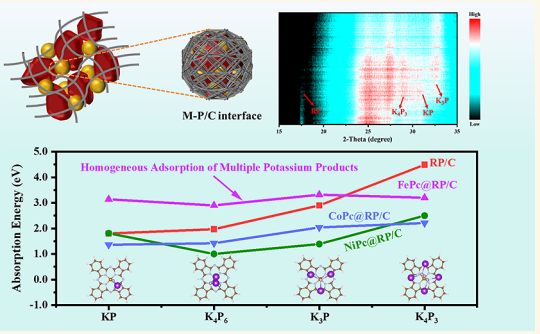

KEYWORDS: *potassium ion batteries, red phosphorus, metal phthalocyanine, phosphorus−carbon composites, multiple potassiation products*

INTRODUCTION

Lithium-ion batteries have been widely used in mobile electronic devices, though they are still facing many challenges due to the lack of lithium resources.[1−3] In recent years, potassium ion batteries (PIBs) have received widespread recognition as emerging technologies for the storage of energy. With more abundant resources in the earth's crust (2.09 wt % of potassium vs 0.0017 wt % of lithium) and the redox potential of K^+/K (−2.93 V vs SHE) is very close to that of Li^+/Li (−3.04 V vs SHE), so PIBs have significant potential for energy storage.[4−7] Graphite, as a typical intercalation-type carbon-based material for PIBs, has a low theoretical specific capacity (only 279 mAh g^{-1}) due to its intercalation mechanisms for storing potassium ions.[8,9] In contrast, phosphorus is a superior alloy material that can provide a theoretical specific capacity of 865 mAh g^{-1} (based on the formation of KP), which has attracted much attention.[2,10] Among three isomers of phosphorus, red phosphorus (RP) is widely used in the research of the anode of PIBs due to its cheapness and excellent chemical stability,[11−13] while white phosphorus is highly toxic and flammable in humid air, and black phosphorus is difficult to be prepared and expensive.[14]

However, RP is accompanied by huge volume expansion in the process of repeated potassiation/depotassiation, which causes the pulverization of RP and rapid capacity decay. The low conductivity (10^{-14} S cm^{-1}) greatly limits its electrochemical capacity and rate performance.[15] In order to alleviate the above problems, one of the most effective approaches is to hybridize RP and carbon materials. Currently, the primary

Received: April 1, 2024
Revised: June 1, 2024
Accepted: June 11, 2024
Published: June 19, 2024

Downloaded via WUHAN UNIV OF TECHNOLOGY on September 6, 2025 at 05:34:38 (UTC).
See https://pubs.acs.org/sharingguidelines for options on how to legitimately share published articles.

© 2024 American Chemical Society

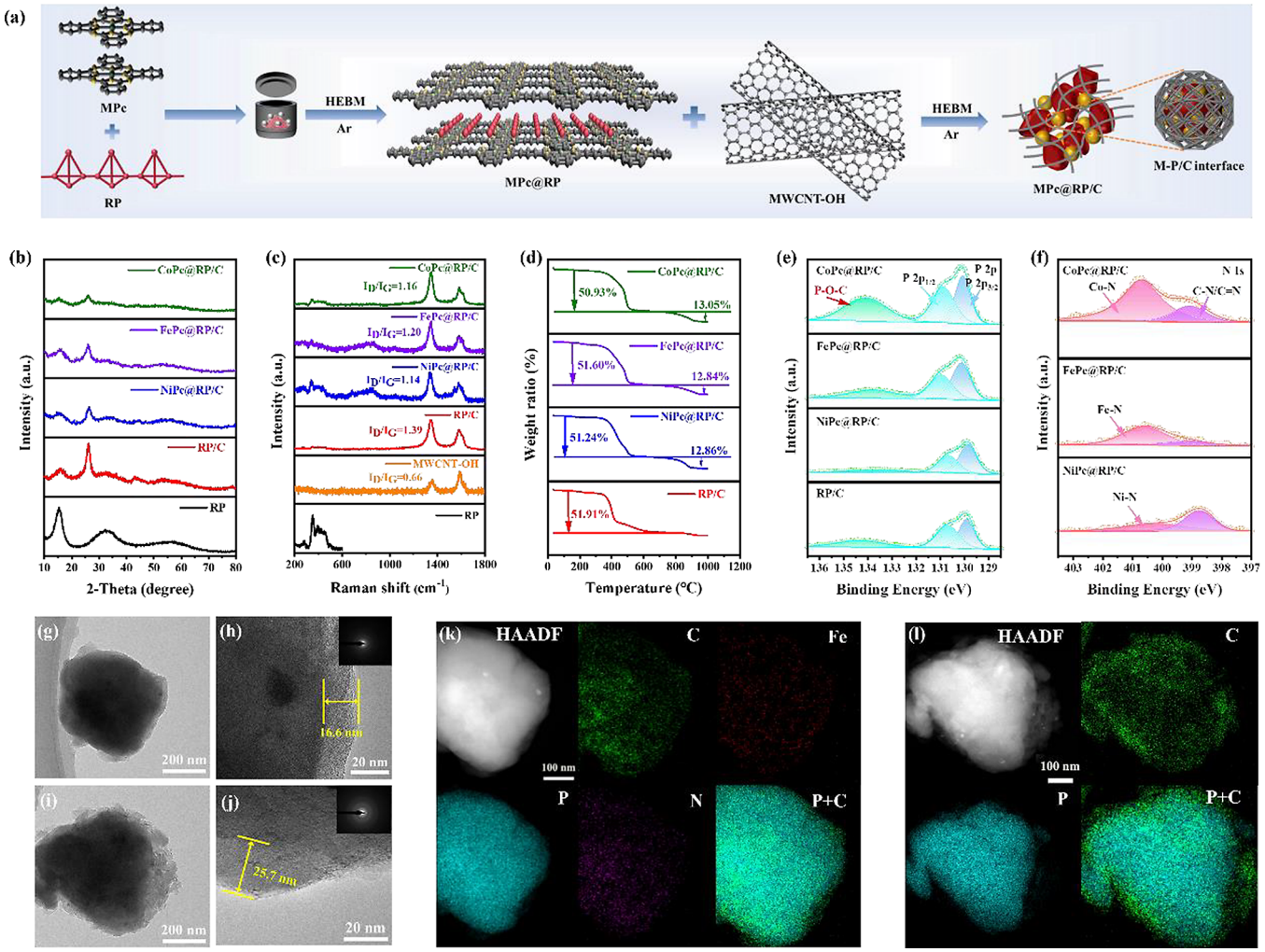

Figure 1. (a) Schematic diagram of the stepwise ball milling preparation process of MPc@RP/C. (b) XRD patterns of MPc@RP/C, RP/C, and RP. (c) Raman mapping of MPc@RP/C, RP/C, MWCNT−OH, and RP. (d) Thermogravimetric analysis plots of MPc@RP/C and RP/C. (e) P 2p XPS spectra of the MPc@RP/C and RP/C. (f) N 1s XPS spectra of the MPc@RP/C. (g) TEM images of FePc@RP/C. (h) HRTEM images of FePc@RP/C (inset: the SAED pattern). (i) TEM images of RP/C. (j) HRTEM images of RP/C (inset: the SAED pattern). (k) EDS elemental mapping diagrams of FePc@RP/C. (l) EDS elemental mapping diagrams of RP/C.

methods for producing phosphorus−carbon composites are ball milling and evaporation condensation. The preparation of phosphorus−carbon composites through evaporation condensation will inevitably lead to a white phosphorus residue during the cooling process. The presence of white phosphorus can significantly impact battery safety.[14] Although Tuan et al. manufactured a composite electrode by ball milling a mixture of RP, multiwall carbon nanotubes, Ketjen black and binder, which had a reversible specific capacity of 750 mAh g^{-1} and a good rate performance of 300 mAh g^{-1} at 1 A g^{-1},[11] the direct ball milling of RP and carbon materials can result in incomplete coverage of RP particles by carbon materials, leading to the inactivation of active substances and the generation of "dead phosphorus", which still presents a challenge to prepare highly stable RP anode composite.

Metal phthalocyanine (MPc) is a type of metal macrocyclic chelate. It has a graphite-like $\pi-\pi$ conjugated structure and a highly efficient electrocatalytic active site M-N_4 structure. MPc is chemically and physically stable, making it a highly efficient and stable electrocatalyst. For instance, Lee and co-workers designed a multifunctional polymeric cobalt phthalocyanine molecule with triethylene glycol linkers (TCP) and loaded it onto carbon nanotubes to obtain TCP/MCs.[16] Electrochemical and theoretical analyses verified that cobalt ions in the phthalocyanine center can provide redox mediating capacity, which facilitates the kinetics of polysulfide uptake and conversion reactions. Additionally, the nitrogen atom displays a strong polar interaction with Li, resulting in a lithophilic effect. As both RP and sulfur are promising alloy conversion electrode materials with similar reaction mechanisms, the study considers the introduction of MPc into phosphorus−carbon composites to address the challenges faced by RP anodes. The MPc can offer following advantages for RP anodes: (1) MPc contains M-N_4 high catalytic activity sites, which can improve the electron transport and electrochemical activity of RP;[17] (2) RP can be compounded with carbon matrix through the $\pi-\pi$ conjugated structure provided by MPc, alleviating the problem of poor adsorption between RP and carbon materials;[16] (3) the MPc can form complexes with K^+ ions, thus homogenize the distribution of K^+ ions though its planar molecule, and increase the mobility number of K^+ ions, further reducing the spatial electric field and inhibiting the generation of potassium dendrites.[17,18] Therefore, the introduction of MPc into phosphorus−carbon

https://doi.org/10.1021/acsnano.4c04344
ACS Nano 2024, 18, 17197−17208

composites can be supposed to realize the organic−inorganic hybridization of RP, carbon materials, and MPc.

Herein, MPc@RP/C composite is prepared by efficient ball milling, in which RP is used as the active center, MPc acts as the "binder" to connect RP with carbon materials and electrocatalyst for electrochemical potassium storage activity, and graphitized hydroxylated multiwalled carbon nanotube (MWCNT−OH) is used as the conductive network of the composite system. It is proven that the generalization of organic−inorganic hybridization among RP, carbon materials, and MPc, through studying effect of the addition of cobalt phthalocyanine (CoPc), iron phthalocyanine (FePc), and nickel phthalocyanine (NiPc). The results showed that the initial Coulombic efficiency (ICE) of MPc@RP/C increased up to 75.5%. In addition, the discharge-specific capacity of FePc@RP/C is 411.9 mAh g^{-1} after 100 cycles at 0.05 A g^{-1} owing to the growth of solid electrolyte interphase (SEI) with high mechanical strength. XPS depth profile analysis reveals that the incorporation of MPc facilitated the formation of K−F bonds and low-valent sulfur species in SEI membranes, which would help to improve the cycle stability of the battery. Besides, density functional theory (DFT) theoretical calculations show that MPc exhibits more homogeneous adsorption energy for multiple potassiation products of the RP anode compared to carbon materials.

RESULTS AND DISCUSSION

Synthesis and Characterization of Materials. MPc@RP/C was prepared through a stepwise ball milling process, as illustrated in Figure 1a. RP and MPc in a mass ratio of 4:1 were sealed in an agate jar through a glovebox filled with argon gas and then ball milled at 500 rpm for 12 h to obtain MPc@RP. The MPc@RP obtained from the first ball milling and MWCNT−OH were then ball milled again at a mass ratio of 7:3 at 500 rpm for 12 h to obtain MPc@RP/C.

Since the central cavity of the phthalocyanine ligand can be coordinated with a variety of transition metal ions, the exploration of MPcs with different central metal ions is essential to optimize the synthesis process of phosphorus−carbon composites. Currently, CoPc, FePc, and NiPc have been extensively investigated as catalysts in the field of lithium−sulfur batteries and catalysis. These three MPcs are linked by a divalent metal ion and four nitrogen atoms to form the M-N_4 electrocatalytic active site. The three metal atoms of iron, cobalt, and nickel all belong to the group VIII elements, which have similar chemical properties. However, due to the different electron arrangements in the 3d orbitals of the three metal atoms, the adsorption capacity of the composites will be affected differently.[19] Therefore, three kinds of MPc, CoPc, FePc, and NiPc were separately used to composite with RP to study their effects in this study.

X-ray diffraction (XRD) patterns of the commercial RP, RP/C, and MPc@RP/C composites are demonstrated in Figure 1b. XRD results show that RP has an amorphous structure, MWCNT−OH and MPc have a good crystalline structure (Figure S1a−d), whereas both the prepared RP/C and MPc@RP/C composites show amorphous properties. After ball milling, the diffraction peaks corresponding to RP and MPc in the prepared MPc@RP/C composites are significantly attenuated, indicating that RP and MPc are successfully encapsulated in carbon materials.[20] The I_D/I_G peak ratio in the Raman spectra can reflect the disorder level of various carbon composites. As shown in Figure 1c, the I_D/I_G ratio of MPc@RP/C is 1.14−1.20, which is much lower than that of RP/C (I_D/I_G is 1.39), indicating that the carbon matrix of MPc@RP/C has a lower disorder. In order to investigate the RP and MPc contents of the composites, thermogravimetric (TG) analysis was performed (Figure 1d). TG analysis tests reveal that the content of RP in the composites is about 51 wt % and the content of MPc is around 13 wt %.

In order to further investigate the role of MPc addition to RP/C composites, X-ray photoelectron spectroscopy (XPS) was performed (Figure 1e,f). The P 2p XPS spectra illustrate that the incorporation of CoPc and FePc promotes the formation of P−O−C bonds, and the promotion effect of CoPc is more pronounced.[21] While the incorporation of NiPc inhibits the growth of P−O−C bonds, which may be related to the structure of MPc with a highly catalytically active site M-N_4. As shown in Figure 1f N 1s XPS spectra,[16] the strengths of Co−N and Fe−N bonds are significantly higher than those of C−N/C═N bonds, while the strengths of Ni−N bonds are significantly weaker than those of C−N/C═N bonds because the two Ni−N bonds formed by the allotropic bonds are partially destroyed during ball milling, and the two Ni−N bonds formed by the covalent bonds are still intact. Namely, the M-N_4 structures in CoPc and FePc remain intact, whereas the M-N_4 structure is partially transformed into the M-N_2 structure in NiPc. Thus, this structural change gives MPc a different effect on the formation of P−O−C bonds.

The micromorphology and structure of samples were analyzed by scanning electron microscope (SEM) (Figure S2a−d). The test results show that MPc@RP/C and RP/C present a few microns in size and irregular lumpy particles. Further investigation of the effect of MPc introduction on carbon layer-coated RP was conducted using transmission electron microscopy (TEM) and energy-dispersive X-ray spectroscopy (EDS) elemental mapping. As shown in Figures 1g,k, S3, and S4, the outer surface of the RP in MPc@RP/C composites showed a thin and uniform distribution of the carbon layer (as shown in Figures 1h, S3b, and S4b, the thicknesses of the carbon layers of the samples are 16.6, 10.4, and 6.9 nm, respectively), and the RP was uniformly coated in the carbon layer, with no RP particles detached from the carbon layer. However, the RP/C composites showed a thick and inhomogeneous distribution of the carbon layer (as shown in Figure 1j, the thicknesses of the carbon layers of RP/C is 25.7 nm), with a few RP particles detached from the whole carbon layer (Figure 1i,l). The reason for this difference is closely related to the fact that MPc has an M-N_4 active site. As shown in Figures 1k,l, S3c, and S4c, since the M-N_4 structure of FePc@RP/C and CoPc@RP/C composites remained intact during ball milling, the carbon layers on their RP surfaces were more uniformly distributed and there was no carbon layer agglomeration. Conversely, the M-N_4 structure of NiPc@RP/C was somewhat disrupted during ball milling, and the carbon layer on its surface exhibited a slight agglomeration phenomenon. Nevertheless, in comparison with RP/C, where the carbon layer was agglomerated on the RP surface, the agglomeration of the carbon layer in MPc@RP/C was significantly suppressed. The thin, uniform, and flat carbon layer would be more conducive to the migration of K^+ and effectively alleviate the huge volume expansion of RP in the process of repeated potassiation/depotassiation, so as to improve the cycle stability of the battery.[22,23] The selected area electron diffraction (SAED) of particles for the composites shows what are typical amorphous halos (Figures

https://doi.org/10.1021/acsnano.4c04344
ACS Nano 2024, 18, 17197−17208

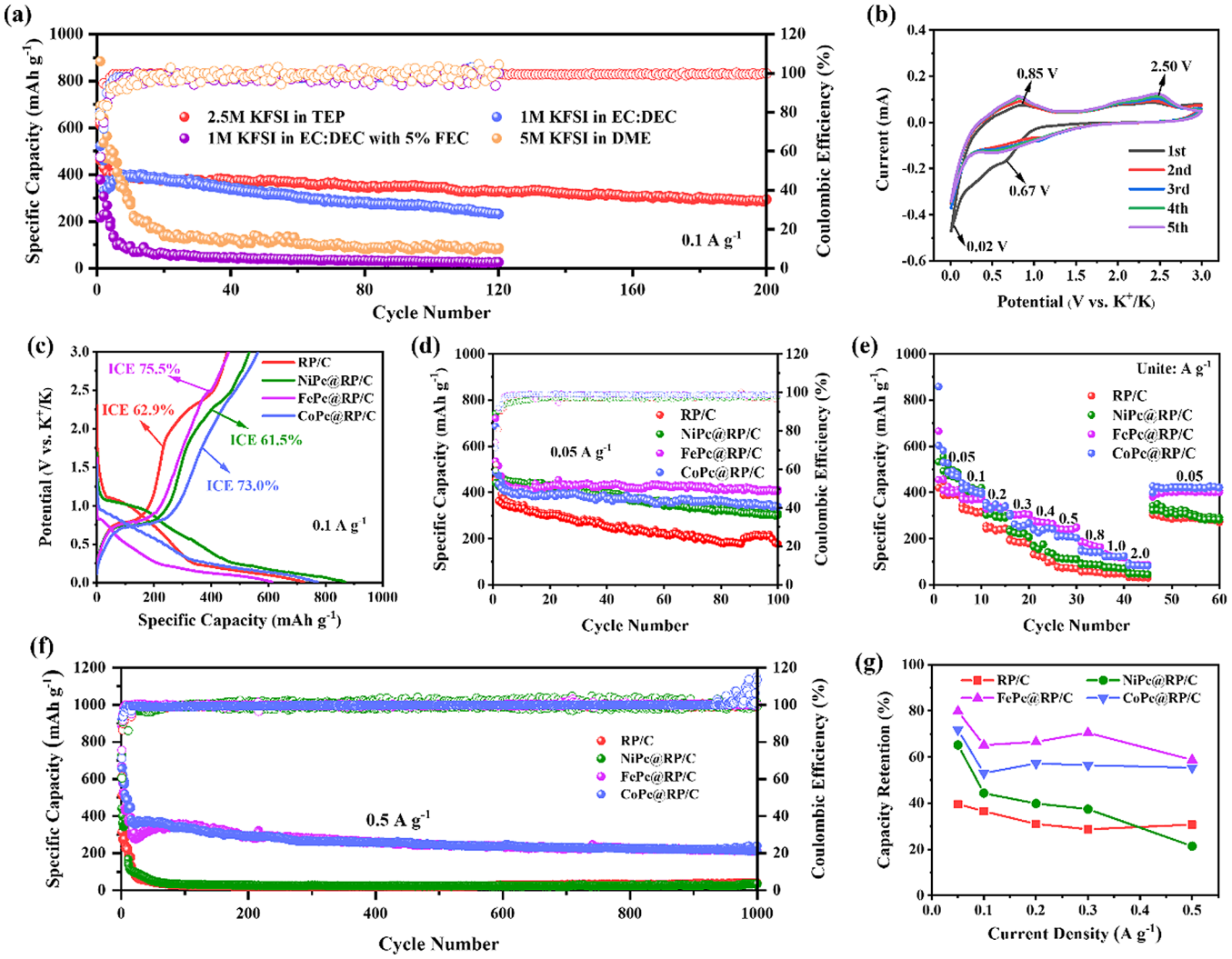

Figure 2. (a) Cycling performance of FePc@RP/C with different electrolytes at a current density of 0.1 A g^{-1}. (b) CV curves at 0.2 mV s^{-1} scan rate of FePc@RP/C. (c) Initial charge/discharge curves and ICE at 0.1 A g^{-1} for samples. (d) Cycling performance of MPc@RP/C and RP/C at 0.05 A g^{-1}. (e) Rate performance of MPc@RP/C and RP/C at different current densities. (f) Cycling performance of MPc@RP/C and RP/C at 0.5 A g^{-1}. (g) Comparison of capacity retention for samples after 100, 200, 350, 400, and 1000 cycles at 0.05, 0.1, 0.2, 0.3, and 0.5 A g^{-1}, respectively.

1l,n, S3c and S4c, insets), which is in concordance with the XRD results that the composites are amorphous. In conclusion, the TEM and EDS elemental mapping analyses demonstrated that MPc anchored on RP successfully induced a uniform distribution of the carbon layer on the RP surface, which effectively addressed the issue of incomplete encapsulation of RP by the carbon layer.

Potassium Storage Performance of MPc@RP/C. Fresh potassium flakes were used as reference and counter electrodes to assemble potassium ion half cells. First, cycling tests were carried out with four different electrolytes at 0.1 A g^{-1} in order to find an electrolyte to match the electrode materials (Figure 2a). Compared to the other three electrolytes, 2.5 M KFSI/TEP has the best cycling stability. 5 M KFSI/DME has a high initial specific capacity but a rapid capacity decline. Although 1 M KFSI/EC:DEC shows good cycling stability, its capacity is significantly lower than that of the 2.5 M KFSI/TEP after 120 cycles. When FEC is added to 1 M KFSI/EC:DEC, the capacity decay is rapid, indicating that the FEC additive has some side effects on the RP anode. In order to exclude the effect of electrolyte chemistry on the suitability of the electrode materials, a series of cycling tests were carried out with different electrolytes at 0.1 A g^{-1}. As shown in Figures 2a and S5, the electrolyte with a concentration of 2.5 M KFSI/TEP has optimal suitability for different composite materials.

Figure 2b presents the cyclic voltammetry (CV) curve of FePc@RP/C at a 0.2 mV s^{-1} scanning rate. During the first cathodic scanning cycle, a broad irreversible cathodic peak appears at 0.67 V due to electrolyte decomposition and the formation of SEI, but the peak disappears in subsequent cycles.[24−26] Upon comparing the cathodic peak widths at 0.67 V in the CV curves (Figure S6a−c) of the four samples, it is evident that FePc@RP/C < CoPc@RP/C < NiPc@RP/C < RP/C, which suggests that the formation of a stable SEI from RP/C requires the consumption of more electrolyte. The results also indicate that the SEI formed in MPc@RP/C composites can reduce the direct contact between RP and electrolyte, thereby inhibiting the occurrence of side reactions.[27] The cathodic peak at 0.02 and 0.67 V corresponds to the reaction of RP with potassium, while the two anodic

https://doi.org/10.1021/acsnano.4c04344
ACS Nano 2024, 18, 17197−17208

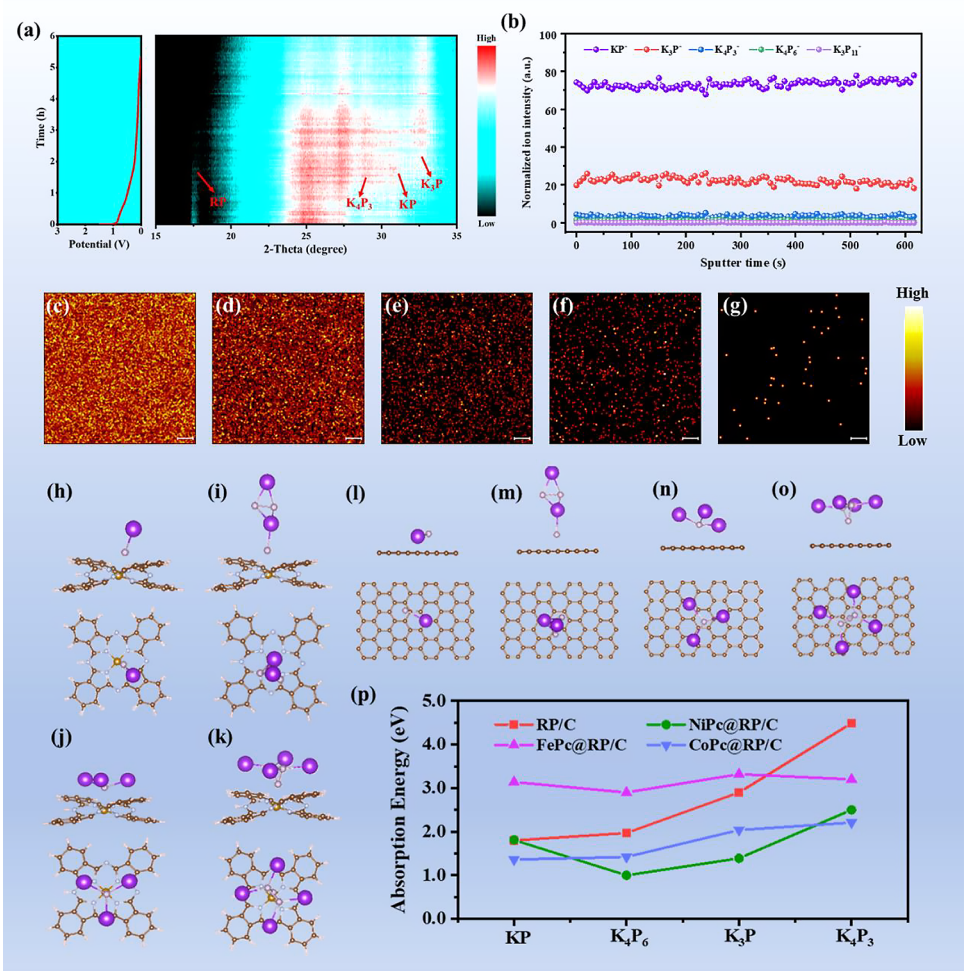

Figure 3. (a) Contour plot of in situ XRD analysis of MPc@RP/C during the initial discharge process and corresponding discharge curve. (b) Normalized ionic strength of five secondary ion fragments (KP^-, KP_3^-, $K_4P_3^-$, $K_4P_6^-$, and $K_3P_{11}^-$) of MPc@RP/C anode in the completely discharged state scanned in depth with sputtering time using TOF-SIMS. (c−g) Thermal imaging distributions of five ion fragments, KP^-, KP_3^-, $K_4P_3^-$, $K_4P_6^-$, and $K_3P_{11}^-$, respectively, for MPc@RP/C anode in the completely discharged state. (h−k) Modeling the adsorption of K_2P_3, K_3P, KP, and K_4P_3 on FePc, respectively. (l−o) Modeling the adsorption of K_2P_3, K_3P, KP, and K_4P_3 on carbon matrix, respectively. (p) Comparison of adsorption energies for K_xP_y between MPc and carbon materials.

peaks at 0.85 and 2.50 V during the anodic scanning process correspond to the depotassiation process. A comparison of the anodic peaks of the samples at these two locations reveals that the two anodic peaks of FePc@RP/C and CoPc@RP/C enhanced with the increase in the number of scans. The anodic peaks of RP/C and NiPc@RP/C at 0.85 V do not change significantly. However, the peaks of RP/C at 2.50 V weaken with the increase in the number of scans, which indicates that the MPc addition enhances the potassiation/depotassiation kinetics and electrochemical activity of the electrode.[28] In addition, the CV curves of the samples exhibit a high degree of overlap during the subsequent scans, indicating that the potassiation/depotassiation process of the electrodes is well reversible. Figure 2c displays the charge/discharge curves and Coulombic efficiency for the first cycle of MPc@RP/C and RP/C at 0.1 A g^{-1}. The first charge/discharge specific capacities of RP/C, NiPc@RP/C, FePc@RP/C, and CoPc@RP/C are 455.9/724.9 (ICE is 62.9%), 533.4/867.9 (ICE is 61.5%), 462/612.3 (ICE is 75.5%), and 563.6/771.8 mAh g^{-1} (ICE is 73.0%), respectively, which once again demonstrates the feasibility of MPc. Figure 2c also shows a similar phenomenon to the CV curve: compared with the RP/C electrode, MPc@RP/C begins to form a SEI film at a lower potential,[27] which indicates that the decomposition activity of the MPc@RP/C surface to the electrolyte is lower than that of the RP/C.

The electrochemical performances of composites were compared after the addition of three different MPcs. As illustrated in Figure 2d, the capacities of FePc@RP/C, CoPc@RP/C, NiPc@RP/C, and RP/C are 411.9, 340.1, 308.7, and 178.3 mAh g^{-1} after 100 cycles at 0.05 A g^{-1} (the average capacity contribution of MWCNT−OH is only 47.0 mAh g^{-1} according to Figure S7), and the capacity retention rates are, respectively, 79.8, 71.7, 65.2, and 39.6%, which verifies the feasibility of MPc added to phosphorus−carbon composites for the benefit of enhancing the cycling stability of batteries. The rate performances of MPc@RP/C and RP/C are shown in Figure 2e. The average discharge-specific capacity of FePc@RP/C at 0.05, 0.1, 0.2, 0.3, 0.4, 0.5, 0.8, 1.0, and 2.0 A g^{-1} are 473.6, 376.3, 338.3, 305.9, 271.1, 243.5, 174.9, 123.6, and 88.0 mAh g^{-1}, respectively. Its reversible discharge-specific capacity is 408.0 mAh g^{-1} after 60 cycles at different current densities when the current is restored to 0.05 A g^{-1}, with a capacity recovery rate of 86.1%. After 60 cycles at different current

https://doi.org/10.1021/acsnano.4c04344
ACS Nano 2024, 18, 17197−17208

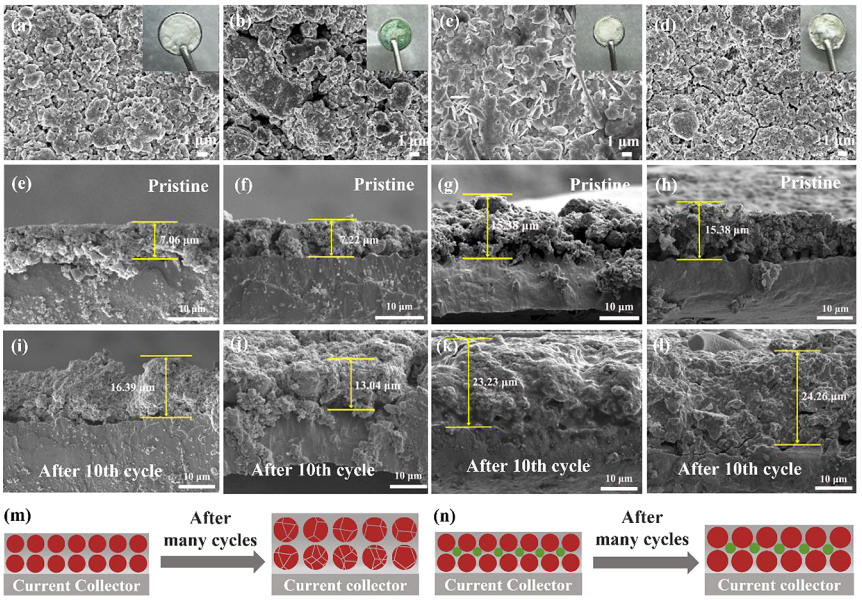

Figure 4. (a–d) Surface SEM images and separator photographs (inset) of RP/C, NiPc@RP/C, FePc@RP/C, and CoPc@RP/C electrode materials after cycling for 10 cycles at 0.1 A g^{-1}. (e–h) Cross-sectional SEM images of RP/C, NiPc@RP/C, FePc@RP/C, and CoPc@RP/C electrode materials before cycling. (i–l) Cross-sectional SEM images of RP/C, NiPc@RP/C, FePc@RP/C, and CoPc@RP/C electrode materials after 10 cycles at 0.1 A g^{-1}. (m) Schematic diagram of the structural changes before and after cycling for RP/C. (n) Schematic diagram of the structural changes before and after cycling for MPc@RP/C.

densities, the capacity recovery rates of CoPc@RP/C, NiPc@RP/C, and RP/C are 72.0, 49.9, and 58.6%, respectively. Therefore, FePc@RP/C exhibits the best rate of performance. The cycling performances of MPc@RP/C and RP/C were tested at 0.5 A g^{-1} to investigate their long cycling capability at high current density. As shown in Figure 2f, the discharge specific capacities of FePc@RP/C, CoPc@RP/C, NiPc@RP/C, and RP/C after 1000 cycles at 0.5 A g^{-1} are 211.1, 210.6, 35.7, and 40.7 mAh g^{-1}, respectively. Both FePc@RP/C and CoPc@RP/C exhibit excellent cycling capabilities at a high current density. Figure 2g shows the capacity retention of four electrode materials after 100, 200, 350, 400, and 1000 cycles at 0.05, 0.1, 0.2, 0.3, and 0.5 A g^{-1} (Figure S8), and the results indicate that FePc@RP/C exhibits the best cycling stability under different current densities.

MPc Mechanism of Action. The in situ XRD was used to further reveal the storage mechanism of potassium ions (Figure 3a). During the initial potassiation process, two diffraction peaks appeared at 29.7° and 31.2°, corresponding to the (130) crystal planes of K_4P_3 and (113) crystal planes of KP, respectively. As the potassiation process progressed, these two peaks gradually weakened, and a new diffraction peak emerged at 32.8°, corresponding to the (110) crystal plane of K_3P.[29,30] When discharged to 0.01 V, the diffraction peaks of the three potassiation products still persisted, indicating that the final potassiation products were a triple coexistence of K_4P_3, K_3P, and KP.[29] In order to further determine the existence form of K^+ after complete potassiation, the binding state of P and K^+ for the MPc@RP/C anode under complete discharge was further detected by time-of-flight secondary ion mass spectrometry (TOF-SIMS). As shown in Figure 3b–g, both K_xP_y secondary ion fragment depth profiling and 2D thermographic distribution maps exhibited KP^- dominated signals,[31] while the presence of significant K_3P^- and $K_4P_3^-$ signals were also detected, indicating that the discharge products did not exist in a single form in the fully potassiation state, but rather a variety of discharge products coexist.

In addition, the adsorption energies of K_xP_y on MPc and the carbon matrix were calculated by first-principles. First, the structural models of MPc and carbon matrix were established, and different potassiation states of K_xP_y were selected to study the differences in K_xP_y adsorption on MPc and carbon matrix (Figures 3h–o, S9a–d, and S10a–d). In order to simplify the modeling process, the most basic structural model has been chosen, which is capable of representing different K_xP_y. Adsorption energy is an important parameter to measure the strength of interaction between molecules or atoms and the substrate. When the adsorption energies of K_xP_y on the same substrate differ significantly, this means that they do not interact with the substrate in a uniform manner. This inhomogeneity may lead to several scenarios: (1) when the adsorption energy is high, the binding of K_xP_y to the substrate is very strong and more energy is required to induce its release, which is detrimental to the depotassiation process of the electrode; (2) when the adsorption energy is low, the bonding of K_xP_y to the substrate is weaker, which may result in the adsorbent groups being detached from the substrate, causing the loss of the active material; (3) when there is a large difference in adsorption energies, it implies an inhomogeneity of the interaction force of K_xP_y with the substrate, which may affect the overall release behavior of K_xP_y by causing it to be released more quickly in certain areas and slower in other areas. Therefore, in order to ensure the effective release of K_xP_y, it is often necessary for the substrate surface to have a relatively uniform adsorption energies in order to achieve a consistent release rate over the entire surface. As shown in Figure 3p, the adsorption energies of different MPc and carbon materials for K_xP_y were compared. The calculated results show that the differences between the highest and lowest adsorption energies for various potassiation products on FePc@RP/C, CoPc@RP/C, NiPc@RP/C, and RP/C are determined to be

https://doi.org/10.1021/acsnano.4c04344
ACS Nano 2024, 18, 17197–17208

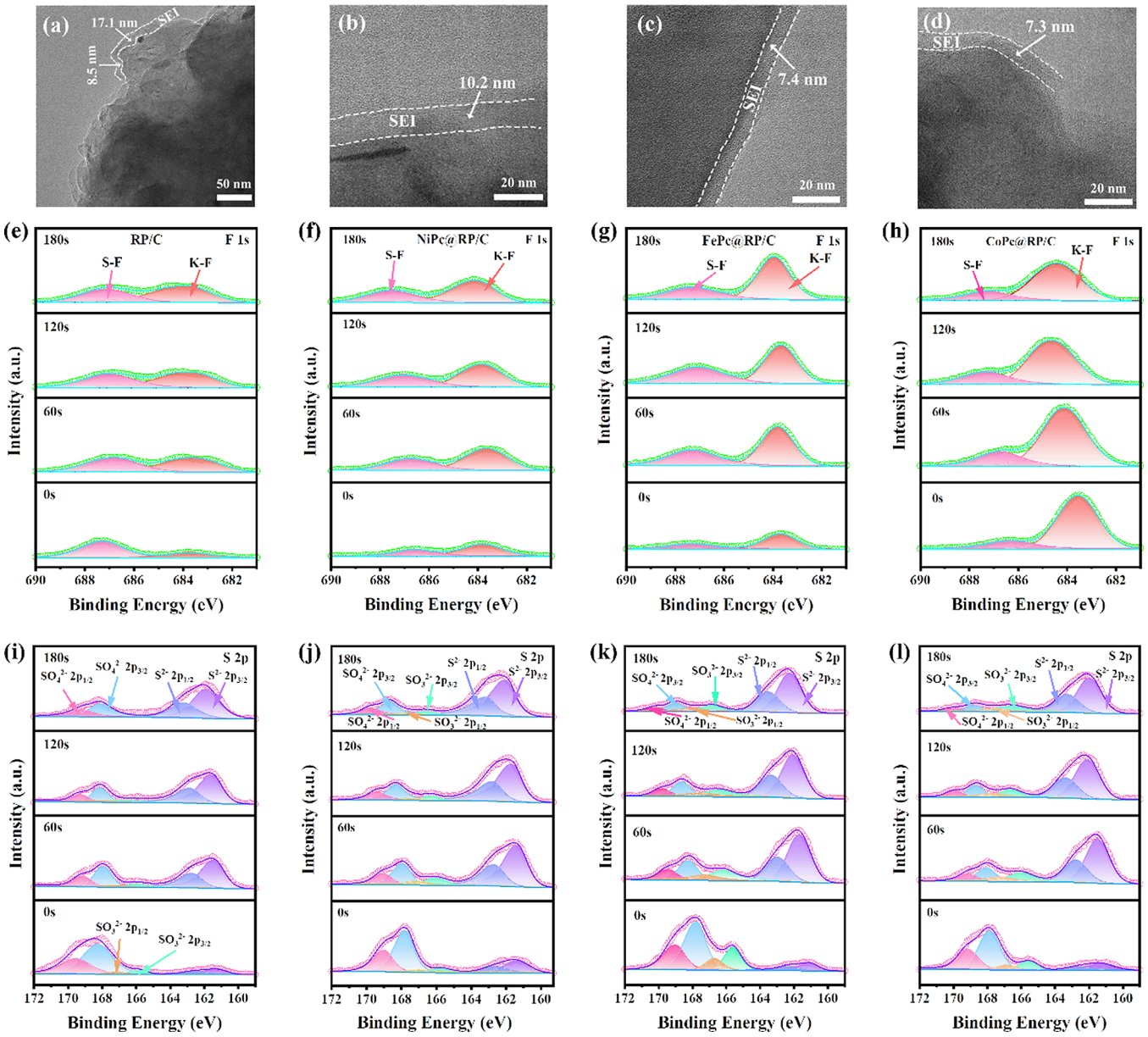

Figure 5. SEI characterization of RP/C and MPc@RP/C after 10 cycles at the current density of 0.1 A g^{-1}. (a−d) HRTEM images of RP/C, NiPc@RP/C, FePc@RP/C, and CoPc@RP/C, respectively. (e−h) F 1s spectra of XPS depth profile analysis for RP/C, NiPc@RP/C, FePc@RP/C, and CoPc@RP/C after 10 cycles, respectively. (i−l) S 2p spectra of XPS depth profile analysis for RP/C, NiPc@RP/C, FePc@RP/C, and CoPc@RP/C after 10 cycles, respectively.

0.41, 0.85, 1.51, and 2.69 eV, respectively. Notably, FePc@RP/C displays the least difference in adsorption energy. This suggests that FePc@RP/C offers a more uniform adsorption behavior toward K_xP_y, which is conducive to the stable and homogeneous release of K_xP_y during the depotassiation process. Consequently, FePc@RP/C exhibits the best electrochemical performance.

The kinetics of potassium ion diffusion during potassiation/depotassiation is a crucial factor that affects the electrochemical performance. Therefore, electrochemical impedance spectroscopy (EIS) was used to study the charge transfer kinetics and K^+ diffusion capacity of the interface. As shown in Figure S11a,b (Table S1), the introduction of MPc results in a significant decrease in the charge transfer resistance (R_{ct}) of MPc@RP/C compared to RP/C, suggesting that MPc can effectively enhance charge separation and transfer during K^+ insertion/extraction.[32] In addition, the calculated σ (Warburg coefficient) value of FePc@RP/C in the low-frequency region is 1185.14 Ω $S^{-1/2}$, which is much smaller than that of RP/C of 2629.30 Ω $S^{-1/2}$, indicating that the diffusion ability of K^+ at the interface is much stronger than that of RP/C.

The surface morphology of the electrode sheet after cycling and the cross-sectional thickness of the electrode sheet before and after cycling were analyzed by SEM to demonstrate that the introduction of MPc can mitigate the volume expansion effect of the electrodes during cycling. The SEM image of the electrode material after cycling is shown in Figure 4a−d. Large particles aggregate on the surface of RP/C and NiPc@RP/C, while the surfaces of FePc@RP/C and CoPc@RP/C remain flat, and there is no obvious aggregation of large particles. However, the aggregation of large particles can easily lead to a significant expansion in the volume of the electrode material

https://doi.org/10.1021/acsnano.4c04344
ACS Nano 2024, 18, 17197−17208

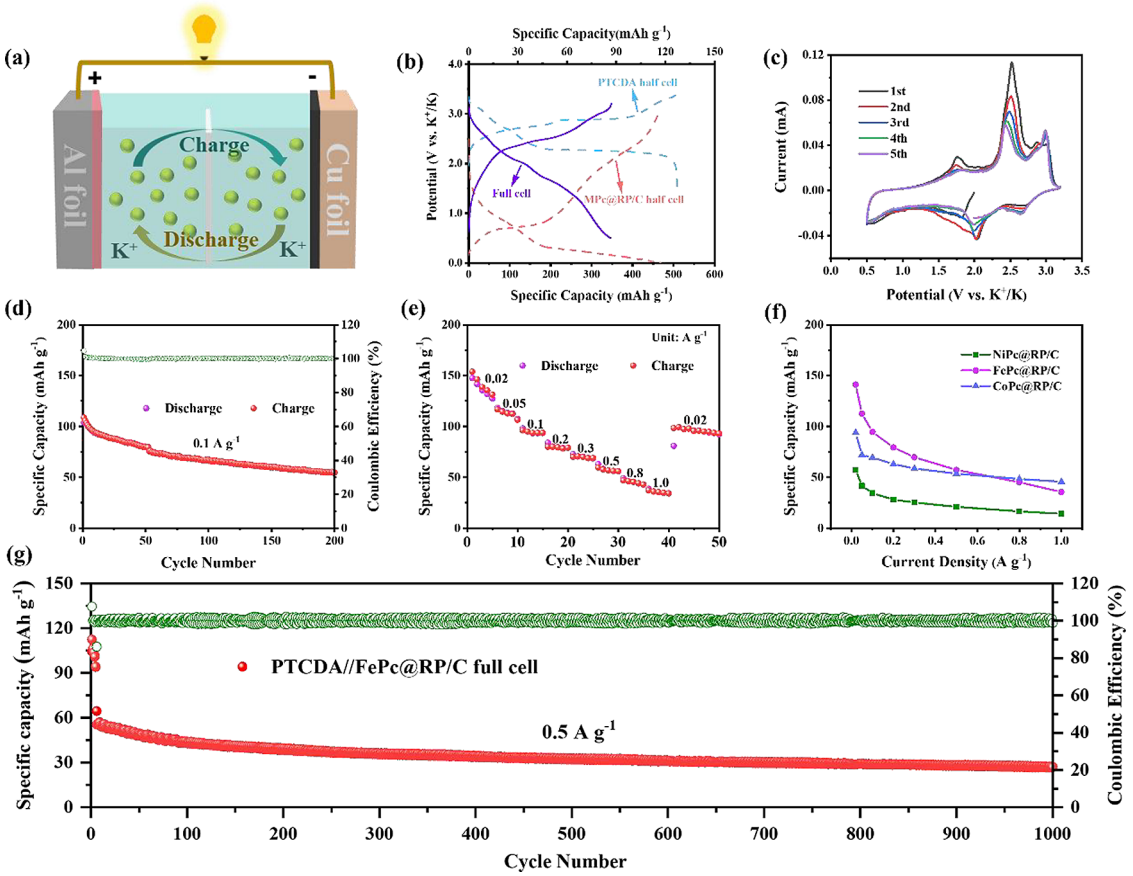

Figure 6. (a) Schematic diagram of PTCDA//MPc@RP/C full cell. (b) Comparison of half and full cell charge/discharge curves. (c) CV curve of PTCDA//MPc@RP/C full cell at the scanning rate of 0.1 mV s^{-1}. (d) Cycling performance of the PTCDA//FePc@RP/C full cell at 0.1 A g^{-1}. (e) Rate performance of PTCDA//FePc@RP/C full cell at different current densities. (f) Comparative plots of the rate performance of PTCDA//NiPc@RP/C, PTCDA//FePc@RP/C, and PTCDA//CoPc@RP/C full cell at different current densities. (g) Cycling performance of PTCDA//FePc@RP/C full cell at 0.5 A g^{-1}.

during the cycle, resulting in a rapid attenuation of battery capacity. As can be seen from the inset (Figure 4b), a large amount of green substance was found on the separator after cycling, but no similar substances were found on the separator of the other three electrode materials, which indicated that NiPc would detach from the composite material during cycling so that NiPc content of electrode material would be greatly reduced, and that NiPc adhered to separator might hinder K^+ migration. Therefore, it is an important reason why the cycling stability of the NiPc@RP/C material is poorer than those of FePc@RP/C and CoPc@RP/C. Given the differences in the thickness of the electrode sheets resulting from their mass loading, we selected electrode sheets with the same mass loads in order to eliminate the effect. The cross-sectional SEM schematics are shown in Figure 4e–h. The cross-sectional thicknesses of RP/C, NiPc@RP/C, FePc@RP/C, and CoPc@RP/C materials before cycling are 7.06, 7.22, 15.38, and 15.38 μm, respectively, and those after cycling are 16.39, 13.04, 23.23, and 24.26 μm, respectively (Figure 4i–l). The volume expansion rates are 132.15, 80.61, 51.14, and 57.74%, respectively. The cross-section SEM images also show that there is no apparent separation between the MPc@RP/C electrode and the collector after cycling. However, there is a separation between the RP/C electrode and the collector, which can lead to a loss of electrical contact between the electrode material and the collector.[28,33] Figure 4m,n shows the structural changes of RP/C and MPc@RP/C before and after cycling. In conclusion, the SEM results demonstrate that the addition of MPc to composites can effectively mitigate the volume expansion of RP during cycling, thereby enhancing the battery's cycle life.

TEM was used to analyze the microstructure of the SEI formed after 10 cycles. This was done to gain insight into the intrinsic mechanism behind the improved battery cycling performance resulting from the addition of MPc to the composites. As shown in Figure 5a–d, the HRTEM images of MPc@RP/C show a thin and uniform SEI, while the HRTEM images of RP/C show a thick and inhomogeneous SEI. In addition to the morphology and structure of SEIs, their chemical composition can have a significant impact on the cycle stability of the battery.[25] Therefore, XPS depth profile analysis was performed on the electrode material after 10 cycles at 0.1 A g^{-1} to reveal the effect of the chemical composition of the SEI on the electrochemical properties. The elements F and S are the signature elements of the electrolyte salt KFSI. Hence, the F 1s and S 2p XPS spectra can be used to assess the effect of redox decomposition of electrolyte salt KFSI on SEI formation. As shown in Figure 5e–h, the F 1s XPS depth profile spectra show two distinct peaks, respectively, the S–F bond near 687.3 eV (originating from undecomposed KFSI) and the K–F bond near 683.7 eV (KF formed by decomposition of KFSI).[25,34−37] When etched for 0 s, the F 1s

https://doi.org/10.1021/acsnano.4c04344
ACS Nano 2024, 18, 17197−17208

spectra show that the S−F bond strength of RP/C is significantly stronger than that of MPc@RP/C, but the K−F bond is significantly weaker than that of MPc@RP/C, suggesting that the introduction of MPc promotes the forward decomposition of the KFSI, resulting in the formation of an inorganic-rich SEI membrane.[25] Comparison of the XPS spectra of F 1s of the three MPcs with different etching times shows that the K−F bond strengths of FePc@RP/C and CoPc@RP/C are significantly stronger than those of NiPc@RP/C, and with the increase of etching time, the K−F bond strength of FePc@RP/C increases slightly while that of CoPc@RP/C decreases significantly. The abundance of K−F bonds gives the SEI membrane strong mechanical strength, which the electrode can buffer volume changes and inhibit the growth of potassium dendrites during cycling.[38,39] Therefore, the cycle stability of FePc@RP/C is better than those of CoPc@RP/C and NiPc@RP/C. The reason for this difference may be related to the partial destruction of the electrocatalytic active site Ni−N_4 of NiPc during the ball milling process.

As shown in Figures 5i−l, the S 2p XPS spectra are able to be categorized into six peaks of SO_4^{2-} $2p_{3/2}$ (SO_4^{2-} $2p_{1/2}$), SO_3^{2-} $2p_{3/2}$ (SO_3^{2-} $2p_{1/2}$), S^{2-} $2p_{3/2}$ (S^{2-} $2p_{1/2}$), which are located at 167.7 (169.0), 165.6 (166.7), and 161.1 eV (162.3 eV).[25,35,40,41] With the increase of etching depth, the composition of sulfur-containing species in the SEI layer shifted from SO_4^{2-} dominated to S^{2-} dominated. At different sputtering times, the amount of low-valent sulfur species at the MPc@RP/C electrodes is significantly higher than that of the RP/C electrode, which suggests that the presence of MPc helps to regulate the production of low-valent sulfur species. Therefore, the increase is beneficial to K^+ migration at the electrode/electrolyte interface.[35] The XPS spectra of P 2p can be divided into two parts (Figure S12), one part is P−P $2p_{3/2}$ and P−P $2p_{1/2}$ produced by RP in the composite at 129.3 and 130.2 eV, respectively, and the other part is P−O $2p_{3/2}$ and P−O $2p_{1/2}$ produced by redox decomposition of the solvent triethyl phosphate (TEP) in the electrolyte at 132.8 and 133.7 eV, respectively.[32,35,42] Upon etching for 0 s, the two peaks corresponding to P−P bonds of RP/C and NiPc@RP/C were observed to be significantly stronger than those of FePc@RP/C and CoPc@RP/C. This suggests that a large number of RP particles were aggregated on the surface of the electrodes following the cycling of RP/C and NiPc@RP/C electrodes. Following etching for 180 s, the peak intensity of the P−P bond was found to be in the order RP/C < NiPc@RP/C < FePc@RP/C < CoPc@RP/C. This indicates that the SEI formed on the surface of the MPc@RP/C composite under the action of MPc is more effective at encapsulating the RP particles inside the electrodes, which also reduces the direct contact between RP and electrolyte. This inhibits the occurrence of side reactions and accommodates the volume change of RP during repeated cycling. In summary, HRTEM and XPS depth profile analysis demonstrated that the addition of MPc to phosphorus−carbon composites contributes to the formation of a superior SEI interface, which promotes K^+ migration at the interfaces and thus improves the cycle stability of the battery.

Full Cell Electrochemical Performance. In order to evaluate the potential of MPc@RP/C electrodes for practical applications, full cells were assembled with the MPc@RP/C anode and PTCDA cathode (Figure 6a). First, the PTCDA electrodes were assembled into potassium ion half cells to examine their electrochemical performance (Figure S13a−c). The results show that it is capable of delivering a specific capacity of 119.0 mAh g^{-1} after 120 cycles at 0.1 A g^{-1}, with 93.6% capacity retention, demonstrating excellent cycling stability. Before assembling full cells, the PTCDA electrode was prepotassiated at 0.02 A g^{-1} for five cycles, and then it was assembled with the activated MPc@RP/C electrode to assemble full cells. Figure 6b compares the charge/discharge curves of the half and full cells, showing that the full cell discharged at an average voltage of 1.80 V. As shown in Figure 6c, the CV curves of the full cell at 0.1 mV s^{-1} have a high degree of overlap, indicating that the assembled full cell has good reversibility.

Figures S14a, S15a and 6d demonstrate that the initial discharge-specific capacities of PTCDA//NiPc@RP/C, PTCDA//CoPc@RP/C, and PTCDA//FePc@RP/C full cells are 50.9, 76.2, and 103.9 mAh g^{-1}, respectively, and the discharge specific capacities after 200 cycles at 0.1 A g^{-1} are 23.0, 50.0, and 54.7 mAh g^{-1}, respectively, showing great application potential. In addition, the full cell rate performances of three kinds of electrode materials are also compared as shown in Figures 6e,f, S14b, and S15b. The PTCDA//FePc@RP/C and PTCDA//CoPc@RP/C can provide discharge-specific capacities of 45.2 and 48.5 mAh g^{-1}, respectively, even at 0.8 A g^{-1}. However, the discharge-specific capacity of PTCDA//NiPc@RP/C is only 16.5 mAh g^{-1} at a rate of 0.8 A g^{-1}. Thus, the result again demonstrates that FePc@RP/C and CoPc@RP/C have superior electrochemical performance than NiPc@RP/C. As shown in Figure 6g, the PTCDA//FePc@RP/C full cell can still provide a discharge-specific capacity of 27.2 mAh g^{-1} after 1000 cycles at 0.5 A g^{-1}. Therefore, MPc@RP/C shows good potential for energy storage applications.

CONCLUSIONS

In summary, the addition of MPc to phosphorus−carbon composites can effectively contribute to the generation of the thin and homogeneous carbon layer on the RP surface, which alleviates the problem of incomplete coverage of the RP by the carbon layer and reduces the generation of "dead phosphorus". Meanwhile, the coexistence of multiple potassiation products (K_xP_y) as the final discharge products from the RP anode has been demonstrated by both in situ XRD and TOF-SIMS. According to density functional theory theoretical calculations, MPc exhibits homogeneous adsorption energy for K_xP_y, which facilitates the uniform desorption of K_xP_y during the depotassiation process. In addition, they also promote the forward decomposition of KFSI and the growth of SEI with a high mechanical strength, which alleviates the volume expansion of RP during repeated cycling. Accordingly, the FePc@RP/C electrode has an ICE of 75.5% at 0.1 A g^{-1}, and a discharge-specific capacity of 411.9 mAh g^{-1} after 100 cycles at 0.05 A g^{-1}, with a capacity retention of 79.8%. Overall, the combination of organic molecules that have a high electrocatalytic activity with high-capacity and huge-volume expansion anodes provides a universal approach for designing PIBs with a high ICE and long cycle life.

MATERIALS AND METHODS

Preparation of the MPc@RP/C. All reagents were used directly after the purchase without further purification. First, RP and MPc at a mass ratio of 4:1 were sealed in an agate ball milling jar (the mass ratio of material and ball milling beads was 1:25) through an argon-filled glovebox and then high-energy ball milling at a rotational speed of 500 rpm for 12 h. After the initial ball milling was completed, the

https://doi.org/10.1021/acsnano.4c04344
ACS Nano 2024, 18, 17197−17208

MPc@RP was isolated in an argon-filled glovebox. To further prepare the MPc@RP/C material, the MPc@RP prepared by the first ball milling and the graphitized MWCNT−OH were sealed in an agate ball milling jar (the mass ratio of the material to the ball milling beads was 1:50) through an argon-filled glovebox according to the mass ratio of 7:3, and then high-energy ball milling at a rotational speed of 500 rpm for 12 h. Here, three different MPc, RP, and MWCNT−OH composites, denoted as CoPc@RP/C, FePc@RP/C, and NiPc@RP/C, respectively, were prepared using the above method.

Preparation of the RP/C. First, the RP was sealed in an agate ball milling jar (the mass ratio of material and ball milling beads was 1:25) through an argon-filled glovebox and then high-energy ball milling at a rotational speed of 500 rpm for 12 h. Then, the RP and MWCNT−OH at a mass ratio of 56:44 (in order to ensure that the RP in the composites is the same) were sealed in an agate ball milling jar (the mass ratio of material and ball milling beads was 1:50) through an argon-filled glovebox, and then again ball milled for 12 h in a planetary ball mill at 500 rpm.

Material Characterization. XRD analysis of the crystal structure was measured on a smart lab diffractometer (Rigaku, Japan). Scanning electron microscopy (SEM) images were collected using a scanning electron JEOL JSM = 7100F microscope (JBOL, Japan). High-resolution transmission electron microscopy (HRTEM), SAED, and energy dispersive spectrometer (EDS) images were collected by utilizing Talos F200S to detect the structure of MPc@RP/C and RP/C. XPS measurements were collected by using a VG Multi Lab 2000 instrument. Raman spectra were recorded on a Renishaw InVia Reflex Raman microscope with an excitation wavelength of 633 nm. TG (STA449F5) was carried out between RT and 1000 °C at a heating rate of 10 °C min^{-1} under N_2 ambient. The TOF-SIMS measurements were conducted with a PHI nano TOF III. A Bi_3^{+2} beam (3 kV, 2 nA) with a raster size of 100 μm was used as the primary beam to detect the samples, sputtering with an Ar^+ beam (2 kV, 100 nA, 400 × 400 μm^2) was applied for depth profiling analysis. The sputtering rate is ∼9.16 nm/min on SiO_2.

Electrochemical Characterization. The anodes were prepared by active materials (80 wt %), super P (10 wt %), and polyvinylidene fluoride (10 wt %) in *N*-methyl-2-pyrrolidone solvent. The mixed slurry was coated on Cu foil and dried at 70 °C under vacuum for 12 h. The mass loading of active materials was 0.6−1.2 mg cm^{-2}. The electrochemical tests were measured by using CR2016 coin cells, which used potassium metal foil as the opposite electrode, GF/D Whatman glass microfiber filter as the separator, and 2.5 M KFSI in TEP as the electrolyte. Constant current charge and discharge tests were carried out by the NEWARE battery testing system in the potential range from 0.01 to 3.0 V (vs K/K^+) at different current densities. The specific capacity of the cells was calculated for all samples based on the total mass of the MPc@RP/C composites. The cycle CV curves and EIS tests (0.1 Hz−100 kHz, 5 mV) were conducted on an electrochemical workstation.

For full-cell assembly, the MPc@RP/C anode was prepotassivated by galvanostatic cycling in potassium half cells between 0.01 and 3.0 V for five cycles at 100 mA g^{-1}. After five cycles, the anode was finally discharged to 0.01 V for full K^+ insertion in the potassium ion half-cell before assembly of the full cell. Then, the K-ion full cells were assembled using the prepotassivated MPc@RP/C as the anode and the preactivated organic perylenetetracarboxylic dianhydride (PTCDA) as the cathode with 2.5 M KFSI in TEP electrolyte. The cells were cycled on the NEWARE battery testing system with a voltage range of 1.5−3.5 V (vs K/K^+) for half cells and 0.5−3.2 V for full cells to perform the charge−discharge tests. The capacity was calculated based on the mass of the cathode. The capacity ratio of the negative electrode to the positive electrode (N/P ratio) is about 1.1−1.4.

In Situ XRD Measurement. In situ XRD experiment was performed on a Bruker D8 Advance XRD. The MPc@RP/C anode was placed behind an X-ray transparent Be window. The sample was scanned from 15° to 35°. The signals were collected in a still mode with a planar detector during the discharge/charge processes, and each pattern was acquired in 110 s with 10 s rest.

EIS Measurement. EIS was further employed to study the interfacial charge transfer kinetics and diffusion behaviors. The diffusion coefficient (D) of K^+ can be investigated by using the following three equations:

$$\omega = 2\pi f$$

$$\mathrm{Zre} = R + \sigma\omega^{-1/2}$$

$$D = \frac{0.5R^2T^2}{A^2n^4F^4C^2\sigma^2}$$

The f is test frequent, R (gas constant) is 8.314 J mol^{-1} K^{-1}, T (Kelvin temperature) is 293.15 K, A is area of electrodes, F (Faraday constant) is 96485 C mol^{-1}, σ is Warburg coefficient, n is electronic transfer number per molecule, and C is molar concentration of K^+.

DFT Calculations. All of the molecular structures are created in Material Studio. We use based on DFT, the Vienna First-Principles Simulation Software Package (VASP) was used for first-principles calculations. The PBE functional is used to describe the exchange-related terms of electrons. The pseudopotential method is used to deal with the nuclear and valence electrons in the system. The kinetic energy cut off of electron wave functions is 400 eV. To get accurate ground state electrons, the geometry optimization was performed by using the conjugate gradient method and the convergence threshold was set to be 10^{-8} eV in energy. The reciprocal space K point is sampled by the gamma method, and the value is set to 3 × 3 × 1. The DFT-D method was employed to accurately describe the van der Waals interactions in the systems. The energy of adsorption can be expressed by the following equation: $E_{ads} = -(E_{ab} - E_a - E_b)$, where E_{ab} is the energy of the substrate adsorbed with adsorbates, E_a is the energy of the substrate, and E_b is the energy of the adsorbates.

ASSOCIATED CONTENT

Supporting Information

The Supporting Information is available free of charge at https://pubs.acs.org/doi/10.1021/acsnano.4c04344.

XRD patterns; XPS spectra; SEM images; TEM images; EDS analysis; CV curves; cycling performance; modeling the adsorption of K_2P_3, K_3P, KP, and K_4P_3 on MPc; EIS curves; and rate performance of full cell (PDF)

AUTHOR INFORMATION

Corresponding Authors

Wen Luo − *Department of Physics, School of Science, Wuhan University of Technology, Wuhan 430070, P. R. China;* orcid.org/0000-0002-1732-295X; Email: luowen_1991@whut.edu.cn

Xiaobin Liao − *State Key Laboratory of Advanced Technology for Materials Synthesis and Processing, School of Materials Science and Engineering, Wuhan University of Technology, Wuhan 430070, P. R. China*; Email: liaoxiaobin@live.com

Liqiang Mai − *State Key Laboratory of Advanced Technology for Materials Synthesis and Processing, School of Materials Science and Engineering, Wuhan University of Technology, Wuhan 430070, P. R. China*; Email: mlq518@whut.edu.cn

Authors

Feiyue Wang − *State Key Laboratory of Advanced Technology for Materials Synthesis and Processing, School of Materials Science and Engineering, Wuhan University of Technology, Wuhan 430070, P. R. China*

Tong Yang − *State Key Laboratory of Advanced Technology for Materials Synthesis and Processing, School of Materials Science and Engineering, Wuhan University of Technology, Wuhan 430070, P. R. China*

Wencong Feng − *State Key Laboratory of Advanced Technology for Materials Synthesis and Processing, School of Materials Science and Engineering, Wuhan University of Technology, Wuhan 430070, P. R. China*
Jingke Ren − *State Key Laboratory of Advanced Technology for Materials Synthesis and Processing, School of Materials Science and Engineering, Wuhan University of Technology, Wuhan 430070, P. R. China*
Xingbao Chen − *State Key Laboratory of Advanced Technology for Materials Synthesis and Processing, School of Materials Science and Engineering, Wuhan University of Technology, Wuhan 430070, P. R. China*
Chaojie Cheng − *State Key Laboratory of Advanced Technology for Materials Synthesis and Processing, School of Materials Science and Engineering, Wuhan University of Technology, Wuhan 430070, P. R. China*

Complete contact information is available at: https://pubs.acs.org/10.1021/acsnano.4c04344

Notes

The authors declare no competing financial interest.

ACKNOWLEDGMENTS

The authors greatly appreciate the financial support from the National Key Research and Development Program of China (Nos. 2022YFB2404300 and 2020YFA0715000), and the National Natural Science Foundation of China (Nos. 52273231).

REFERENCES

(1) Zhou, M.; Bai, P.; Ji, X.; Yang, J.; Wang, C.; Xu, Y. Electrolytes and Interphases in Potassium Ion Batteries. *Adv. Mater.* **2021**, *33*, No. 2003741.
(2) Wu, Y.; Huang, H.; Feng, Y.; Wu, Z.; Yu, Y. The Promise and Challenge of Phosphorus-Based Composites as Anode Materials for Potassium-Ion Batteries. *Adv. Mater.* **2019**, *31* (50), No. 1901414.
(3) Wu, S.; Song, Y.; Lu, C.; Yang, T.; Yuan, S.; Tian, X.; Liu, Z. High-Rate Soft Carbon Anode in Potassium Ion Batteries: The Role of Chemical Structures of Pitches. *Carbon* **2023**, *203*, 211−220.
(4) Li, F.; He, J.; Liu, J.; Wu, M.; Hou, Y.; Wang, H.; Qi, S.; Liu, Q.; Hu, J.; Ma, J. Gradient Solid Electrolyte Interphase and Lithium-Ion Solvation Regulated by Bisfluoroacetamide for Stable Lithium Metal Batteries. *Angew. Chem. Int. Ed* **2021**, *60* (12), 6600−6608.
(5) Ma, L.; Lv, Y.; Wu, J.; Xia, C.; Kang, Q.; Zhang, Y.; Liang, H.; Jin, Z. Recent Advances in Anode Materials for Potassium-Ion Batteries: A Review. *Nano Res.* **2021**, *14* (12), 4442−4470.
(6) Rajagopalan, R.; Tang, Y.; Ji, X.; Jia, C.; Wang, H. Advancements and Challenges in Potassium Ion Batteries: A Comprehensive Review. *Adv. Funct. Mater.* **2020**, *30* (12), No. 1909486.
(7) Hu, X.; Liu, Y.; Chen, J.; Yi, L.; Zhan, H.; Wen, Z. Fast Redox Kinetics in Bi-Heteroatom Doped 3D Porous Carbon Nanosheets for High-Performance Hybrid Potassium-Ion Battery Capacitors. *Adv. Energy Mater.* **2019**, *9* (42), No. 1901533.
(8) Huang, X. L.; Zhao, F.; Qi, Y.; Qiu, Y.-A.; Chen, J. S.; Liu, H. K.; Dou, S. X.; Wang, Z. M. Red Phosphorus: A Rising Star of Anode Materials for Advanced K-Ion Batteries. *Energy Storage Materials* **2021**, *42*, 193−208.
(9) Qian, Y.; Li, Y.; Yi, Z.; Zhou, J.; Pan, Z.; Tian, J.; Wang, Y.; Sun, S.; Lin, N.; Qian, Y. Revealing the Double-Edged Behaviors of Heteroatom Sulfur in Carbonaceous Materials for Balancing K-Storage Capacity and Stability. *Adv. Funct. Mater.* **2021**, *31* (8), No. 2006875.
(10) Sui, Y.; Zhou, J.; Wang, X.; Wu, L.; Zhong, S.; Li, Y. Recent Advances in Black-Phosphorus-Based Materials for Electrochemical Energy Storage. *Mater. Today* **2021**, *42*, 117−136.
(11) Chang, W.; Wu, J.; Chen, K.; Tuan, H. Red Phosphorus Potassium-Ion Battery Anodes. *Adv. Sci.* **2019**, *6* (9), No. 1801354.
(12) Sun, J.; Zheng, G.; Lee, H.-W.; Liu, N.; Wang, H.; Yao, H.; Yang, W.; Cui, Y. Formation of Stable Phosphorus−Carbon Bond for Enhanced Performance in Black Phosphorus Nanoparticle−Graphite Composite Battery Anodes. *Nano Lett.* **2014**, *14* (8), 4573−4580.
(13) Zhou, J.; Ye, W.; Lian, X.; Shi, Q.; Liu, Y.; Yang, X.; Liu, L.; Wang, D.; Choi, J.-H.; Sun, J.; Yang, R.; Wang, M.-S.; Rummeli, M. H. Advanced Red Phosphorus/Carbon Composites with Practical Application Potential for Sodium Ion Batteries. *Energy Storage Materials* **2022**, *46*, 20−28.
(14) Zhang, S.; Liu, C.; Wang, H.; Wang, H.; Sun, J.; Zhang, Y.; Han, X.; Cao, Y.; Liu, S.; Sun, J. A Covalent P−C Bond Stabilizes Red Phosphorus in an Engineered Carbon Host for High-Performance Lithium-Ion Battery Anodes. *ACS Nano* **2021**, *15*, 3365.
(15) Feng, W.; Wang, H.; Jiang, Y.; Zhang, H.; Luo, W.; Chen, W.; Shen, C.; Wang, C.; Wu, J.; Mai, L. A Strain-Relaxation Red Phosphorus Freestanding Anode for Non-Aqueous Potassium Ion Batteries. *Adv. Energy Mater.* **2022**, *12* (7), No. 2103343.
(16) Kim, Y.; Kim, W. I.; Park, H.; Kim, J. S.; Cho, H.; Yeon, J. S.; Kim, J.; Kim, Y.; Lee, J.; Park, H. S. Multifunctional Polymeric Phthalocyanine-Coated Carbon Nanotubes for Efficient Redox Mediators of Lithium−Sulfur Batteries. *Adv. Energy Mater.* **2023**, *13* (22), No. 2204353.
(17) Wang, H.-G.; Wang, H.; Li, Y.; Wang, Y.; Si, Z. A Bipolar Metal Phthalocyanine Complex for Sodium Dual-Ion Battery. *Journal of Energy Chemistry* **2021**, *58*, 9−16.
(18) Dai, H.; Dong, J.; Wu, M.; Hu, Q.; Wang, D.; Zuin, L.; Chen, N.; Lai, C.; Zhang, G.; Sun, S. Cobalt-Phthalocyanine-Derived Molecular Isolation Layer for Highly Stable Lithium Anode. *Angew. Chem. Int. Ed* **2021**, *60* (36), 19852−19859.
(19) Song, X.; Zhou, F.; Yao, M.; Hao, C.; Qiu, J. Insights into the Anchoring of Polysulfides and Catalytic Performance by Metal Phthalocyanine Covalent Organic Frameworks as the Cathode in Lithium−Sulfur Batteries. *ACS Sustainable Chem. Eng.* **2020**, *8* (27), 10185−10192.
(20) Han, X.; Zhang, Z.; Han, M.; Cui, Y.; Sun, J. Fabrication of Red Phosphorus Anode for Fast-Charging Lithium-Ion Batteries Based on TiN/TiP2-Enhanced Interfacial Kinetics. *Energy Storage Materials* **2020**, *26*, 147−156.
(21) Peng, D.; Chen, Y.; Ma, H.; Zhang, L.; Hu, Y.; Chen, X.; Cui, Y.; Shi, Y.; Zhuang, Q.; Ju, Z. Enhancing the Cycling Stability by Tuning the Chemical Bonding between Phosphorus and Carbon Nanotubes for Potassium-Ion Battery Anodes. *ACS Appl. Mater. Interfaces* **2020**, *12* (33), 37275−37284.
(22) Liu, Y.; Liu, Q.; Jian, C.; Cui, D.; Chen, M.; Li, Z.; Li, T.; Nilges, T.; He, K.; Jia, Z.; Zhou, C. Red-Phosphorus-Impregnated Carbon Nanofibers for Sodium-Ion Batteries and Liquefaction of Red Phosphorus. *Nat. Commun.* **2020**, *11* (1), 2520.
(23) Wang, J.; Xu, Y.; Niu, Y.; Liu, Y.; Yao, X. Lithium-Ion Conductivity Epitaxial Layer Contributing to the Structure and Cycling Stability of $LiMn_2O_4$ Cathodes. *ACS Sustainable Chem. Eng.* **2023**, *11* (14), 5408−5419.
(24) Huang, X.; Sui, X.; Ji, W.; Wang, Y.; Qu, D.; Chen, J. From Phosphorus Nanorods/C to Yolk−Shell P@hollow C for Potassium-Ion Batteries: High Capacity with Stable Cycling Performance. *J. Mater. Chem. A* **2020**, *8* (16), 7641.
(25) Xiao, W.; Shi, P.; Li, Z.; Xie, C.; Qin, J.; Yang, H.; Wang, J.; Li, W.; Zhang, J.; Li, X. Regulating Solid Electrolyte Interphases on Phosphorus/Carbon Anodes via Localized High-Concentration Electrolytes for Potassium-Ion Batteries. *Journal of Energy Chemistry* **2023**, *78*, 589−605.
(26) Liu, Z.; Wu, S.; Song, Y.; Yang, T.; Ma, Z.; Tian, X.; Liu, Z. Non-Negligible Influence of Oxygen in Hard Carbon as an Anode Material for Potassium-Ion Batteries. *ACS Appl. Mater. Interfaces* **2022**, *14* (42), 47674−47684.
(27) Zhang, J.; Zhang, K.; Yang, J.; Wing-hei Lau, V.; Lee, G.-H.; Park, M.; Kang, Y.-M. Engineering Solid Electrolyte Interphase on

Red Phosphorus for Long-Term and High-Capacity Sodium Storage. *Chem. Mater.* **2020**, *32* (1), 448−458.
(28) Guan, J.; Rao, A. M.; Zhou, J.; Yu, X.; Lu, B. Structure-Optimized Phosphorene for Super-Stable Potassium Storage. *Adv. Funct. Mater.* **2022**, *32* (31), No. 2203522.
(29) Zhou, E.; Luo, X.; Jin, H.; Wang, C.; Lu, Z.; Xie, Y.; Zhou, S.; Chen, Y.; He, Z.; Ma, R.; Zhang, W.; Xie, H.; Jiao, S.; Lin, Y.; Bin, D.-S.; Huang, R.; Wu, X.; Kong, X.; Ji, H. Breaking Low-Strain and Deep-Potassiation Trade-Off in Alloy Anodes via Bonding Modulation for High-Performance K-Ion Batteries. *J. Am. Chem. Soc.* **2024**, *146* (7), 4752−4761.
(30) Yang, H.; He, F.; Liu, F.; Sun, Z.; Shao, Y.; He, L.; Zhang, Q.; Yu, Y. Simultaneous Catalytic Acceleration of White Phosphorus Polymerization and Red Phosphorus Potassiation for High-Performance Potassium-Ion Batteries. *Adv. Mater.* **2024**, *36* (3), No. 2306512.
(31) Zhao, X.; Geng, S.; Zhou, T.; Wang, Y.; Tang, S.; Qu, Z.; Wang, S.; Zhang, X.; Xu, Q.; Yuan, B.; Ouyang, Z.; Peng, H.; Tang, S.; Sun, H. Unlocking Deep and Fast Potassium-Ion Storage through Phosphorus Heterostructure. *Small* **2023**, *19* (36), No. 2301750.
(32) Wu, X.; Wang, H.; Zhao, Z.; Huang, B. Interstratification-Assembled 2D Black Phosphorene and V_2CT_x MXene as Superior Anodes for Boosting Potassium-Ion Storage. *J. Mater. Chem. A* **2020**, *8* (25), 12705−12715.
(33) Capone, I.; Aspinall, J.; Darnbrough, E.; Zhao, Y.; Wi, T.-U.; Lee, H.-W.; Pasta, M. Electrochemo-Mechanical Properties of Red Phosphorus Anodes in Lithium, Sodium, and Potassium Ion Batteries. *Matter* **2020**, *3* (6), 2012−2028.
(34) Fan, L.; Xie, H.; Hu, Y.; Caixiang, Z.; Rao, A. M.; Zhou, J.; Lu, B. A Tailored Electrolyte for Safe and Durable Potassium Ion Batteries. *Energy Environ. Sci.* **2023**, *16* (1), 305−315.
(35) Liu, C.; Yang, Z.; Sun, J. Synergistic Strategy of the Phosphorus Anode Decorated by LiF and Combined with KFSI-Based Electrolyte against Shuttle Effect of Dissoluble Polyphosphides for Boosting Potassium-Storage Performance. *Energy Storage Materials* **2022**, *53*, 22−31.
(36) Wang, H.; Yu, D.; Wang, X.; Niu, Z.; Chen, M.; Cheng, L.; Zhou, W.; Guo, L. Electrolyte Chemistry Enables Simultaneous Stabilization of Potassium Metal and Alloying Anode for Potassium-Ion Batteries. *Angew. Chem. Int. Ed* **2019**, *58* (46), 16451−16455.
(37) Yang, F.; Hao, J.; Long, J.; Liu, S.; Zheng, T.; Lie, W.; Chen, J.; Guo, Z. Achieving High-Performance Metal Phosphide Anode for Potassium Ion Batteries via Concentrated Electrolyte Chemistry. *Adv. Energy Mater.* **2021**, *11* (6), No. 2003346.
(38) Tang, M.; Dong, S.; Wang, J.; Cheng, L.; Zhu, Q.; Li, Y.; Yang, X.; Guo, L.; Wang, H. Low-Temperature Anode-Free Potassium Metal Batteries. *Nat. Commun.* **2023**, *14* (1), 6006.
(39) Chen, K.-T.; Tuan, H.-Y. Bi−Sb Nanocrystals Embedded in Phosphorus as High-Performance Potassium Ion Battery Electrodes. *ACS Nano* **2020**, *14*, 11648.
(40) Ji, S.; Li, J.; Li, J.; Song, C.; Wang, S.; Wang, K.; Hui, K. S.; Zha, C.; Zheng, Y.; Dinh, D. A.; Chen, S.; Zhang, J.; Mai, W.; Tang, Z.; Shao, Z.; Hui, K. N. Dynamic Reversible Evolution of Solid Electrolyte Interface in Nonflammable Triethyl Phosphate Electrolyte Enabling Safe and Stable Potassium-Ion Batteries. *Adv. Funct. Mater.* **2022**, *32* (28), No. 2200771.
(41) Li, K.; Ma, G.; Yu, D.; Luo, W.; Li, J.; Qin, L.; Huang, Y.; Chen, D. A High-Concentrated and Nonflammable Electrolyte for Potassium Ion-Based Dual-Graphite Batteries. *Nano Res.* **2023**, *16* (5), 6353−6360.
(42) Fang, K.; Liu, D.; Xiang, X.; Zhu, X.; Tang, H.; Qu, D.; Xie, Z.; Li, J.; Qu, D. Air-Stable Red Phosphorus Anode for Potassium/Sodium-Ion Batteries Enabled through Dual-Protection Design. *Nano Energy* **2020**, *69*, No. 104451.

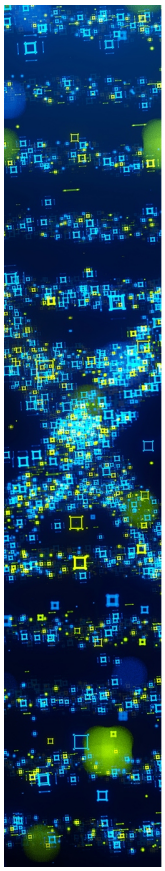
CAS BIOFINDER DISCOVERY PLATFORM™
STOP DIGGING THROUGH DATA —START MAKING DISCOVERIES
CAS BioFinder helps you find the right biological insights in seconds
Start your search
CAS
A division of the American Chemical Society

https://doi.org/10.1021/acsnano.4c04344
ACS Nano 2024, 18, 17197−17208